ACS NANO

www.acsnano.org

ARTICLE

Electrical Tunability of Quantum-Dot-in-Perovskite Solids

Md Azimul Haque,[‖] Tong Zhu,[‖] Roba Tounesi, Seungjin Lee, Maral Vafaie, Luis Huerta Hernandez, Bambar Davaasuren, Alessandro Genovese, Edward H. Sargent,* and Derya Baran*

Cite This: *ACS Nano* 2024, 18, 34089−34095

Read Online

ACCESS | Metrics & More | Article Recommendations | Supporting Information

ABSTRACT: **The quantum-dot-in-perovskite matrix (DIM) is an emerging class of semiconductors for optoelectronics enabled by their complementary charge transport properties and stability improvements. However, a detailed understanding of the pure electrical properties in DIM is still in its early stage. Here, we developed PbS quantum dot-in-$CsSnI_3$ matrix solids exhibiting improved electrical properties and enhanced stability. PbS incorporation reduces the tensile strain of DIM films compared to that of pristine $CsSnI_3$, consequently increasing the electrical conductivity. Electrical conductivity is tunable between 20 and 130 S/cm as a function of PbS concentration. Notably, a decoupling of electrical conductivity and Seebeck coefficient is observed upon PbS addition into the perovskite matrix, which is attractive for thermoelectric applications. Density functional theory analysis reveals that at low concentrations of PbS, light holes/electrons govern the overall transport properties in DIM, while heavy holes/electrons begin to dominate as the PbS concentration increases. Understanding the electrical properties would help for designing DIMs with specific properties for various technological applications.**

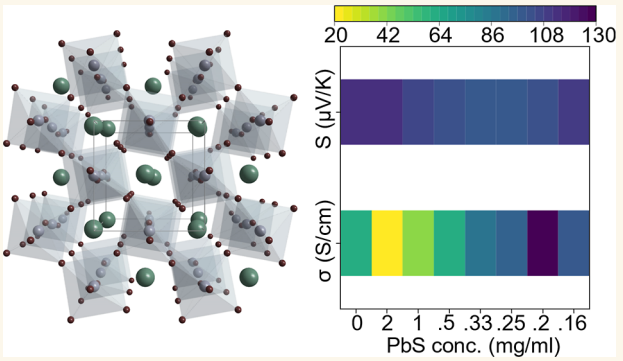

KEYWORDS: *halide perovskite, thermoelectrics, dot-in-matrix, electrical transport, electrical conductivity*

Heterostructures of halide perovskites with various semiconductors are gaining attention due to the synergistic properties exhibited by the composite system. Such heterostructures have been explored for different applications such as photovoltaics, LEDs, field emission devices, and radiation detectors.[1−7] In particular, colloidal quantum dots in a halide perovskite matrix (DIM) are a promising material system owing to the compatible lattice constants, ease of processing, and enhanced optoelectronic properties.[8] DIM materials represent a family of semiconductors that showcase properties absent in individual components and can be categorized into three groups according to the QD composition: chalcogenide QDs in the halide perovskite matrix, elemental QDs in the halide perovskite matrix, and halide perovskite QDs in the halide perovskite matrix.[9,10]

Several studies have demonstrated improved charge transport properties of various QDs in halide perovskite matrices.[11−15] In addition, the introduction of QDs into perovskite matrices has been shown to regulate film formation kinetics and improve DIM stability.[16−18] While the majority of the works on DIM have focused on lead (Pb) halide perovskites for optoelectronic applications, a recent work on DIM involving perovskite QDs in a hybrid tin (Sn) perovskite matrix reported reduced defect density with enhanced photophysical properties and stability.[19] Such DIMs involving Sn perovskites are particularly interesting owing to the instability associated with Sn perovskites.

In the context of Sn perovskites, $CsSnI_3$ has showcased promising performances for thermoelectrics and transistors due to its high electrical conductivity and hole mobility.[20−22] However, the stability of $CsSnI_3$ is limited since it suffers from issues of phase change and Sn-oxidation.[23] Forming DIMs with chalcogenides and a $CsSnI_3$ perovskite matrix may serve as a potential route to improve their electrical properties and stability. Furthermore, the impact of QDs on the electrical properties of halide perovskites beyond optoelectronics remains unexplored. In this work, we report PbS QDs in a

Received: July 21, 2024
Revised: November 13, 2024
Accepted: November 22, 2024
Published: December 6, 2024

https://doi.org/10.1021/acsnano.4c09811
ACS Nano 2024, 18, 34089−34095

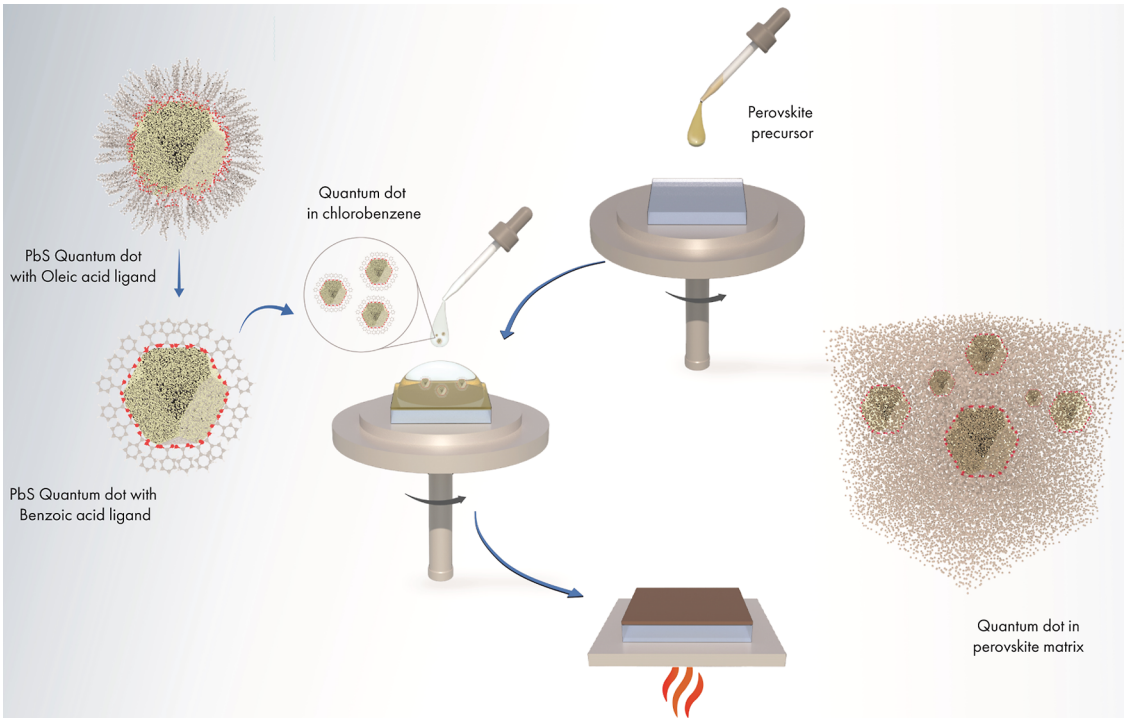

Figure 1. Schematic of the deposition procedure for PbS QDs in the $CsSnI_3$ matrix.

$CsSnI_3$ perovskite matrix and evaluate their carrier transport properties. The inclusion of PbS reduces the tensile strain in $CsSnI_3$ films, leading to an enhanced electrical conductivity of 130 S/cm in contrast to 60 S/cm for pristine $CsSnI_3$ at room temperature. The enhancement in electrical conductivity is due to the improved hole mobility, resulting in overcoming the conductivity−Seebeck trade-off. Density functional theory (DFT) analysis indicated that for low concentrations of QDs in $CsSnI_3$, light holes/electrons dominate the charge transport, contributing to improved electrical properties.

RESULTS AND DISCUSSION

Oleic acid (OA)-capped PbS QDs were ligand-exchanged with short benzoic acid (BA) ligands to improve charge transport.[24] BA-exchanged PbS QDs in chlorobenzene (CB) were incorporated into the $CsSnI_3$ matrix by a single-step spin coating. PbS QDs in CB were introduced as an antisolvent for $CsSnI_3$ during the spin coating process, followed by an annealing treatment to obtain $CsSnI_3$/PbS DIM films. Introducing QDs in the antisolvent step with organic surface ligands eliminates the need for lattice matching between QDs and halide perovskites, offering ease of processing and the ability to form DIMs for a wider range of compositions. Moreover, the QD layer can restrict the surface oxidation of $CsSnI_3$. Figure 1 shows a schematic of the $CsSnI_3$/PbS DIM film formation. PbS incorporation does not disturb the perovskite structure of $CsSnI_3$, and no new phases were observed in X-ray diffraction (XRD) (Figure S1).

The XRD pattern of the PbS QDs is consistent with that of bulk PbS, with broad peaks due to their smaller size (Figure S2). The average size of the PbS QDs was 5 nm, as observed in the high-resolution transmission electron microscopy (HRTEM) images (Figures 2a and S3). The HRTEM investigation confirmed the high crystallinity of the QDs and their pseudospherical morphology. Fourier transform infrared spectroscopy (FTIR) confirmed the significant removal of linear alkanes and alkene C−H stretches from the BA-exchanged QDs (Figure 2b). The $CsSnI_3$/PbS DIM film exhibited stretch from the ligands confirming the presence of PbS (Figures 2c and S4). The top-view scanning electron microscopy (SEM) image of the fresh $CsSnI_3$ film shows prominent pinholes, which are typical of Sn perovskite films without additives.[25] A higher concentration of PbS leads to a larger grain size with PbS present between the grains. For lower concentrations of PbS, the film morphology resembled that of pristine $CsSnI_3$, with a visible presence of PbS on the film surface (Figure S5). The presence of PbS clusters on the $CsSnI_3$/PbS film surface was observed by elemental mapping via SEM−EDX (Figure 2d).

As crystallographic orientation can affect electronic transport, we checked for orientation changes by 2D XRD and found no variations between the pristine and PbS-containing $CsSnI_3$ films (Figure S6). Temperature-dependent in situ XRD demonstrated no change in the phase transition (orthorhombic to tetragonal) temperature of $CsSnI_3$ after PbS addition or heating (Figure 3a,b). Residual strain in perovskite films can affect the charge transport properties. In particular, tensile strain can adversely affect the electrical conductivity of perovskite films.[26] To assess the type and degree of strain in the perovskite films, we performed grazing incident X-ray diffraction (GIXRD) measurements. In general, a shift in the XRD peak to lower angles (θ) indicates tensile strain, whereas a shift in the diffraction peak to higher angles suggests compressive strain.[27] In contrast to pristine $CsSnI_3$ films, $CsSnI_3$/PbS films exhibit lower tensile strain with an almost 2-fold lower θ shift (Figure 3c,d). Hence, the XRD analysis suggests that the addition of QDs in the $CsSnI_3$ matrix might offer improved electronic transport properties.

To determine the transport behavior of the $CsSnI_3$/PbS DIM films, the temperature-dependent electrical conductivity (σ) and Seebeck coefficient (S) of the fresh films were measured. Figure 4a shows the schematic of the measurement

https://doi.org/10.1021/acsnano.4c09811
ACS Nano 2024, 18, 34089−34095

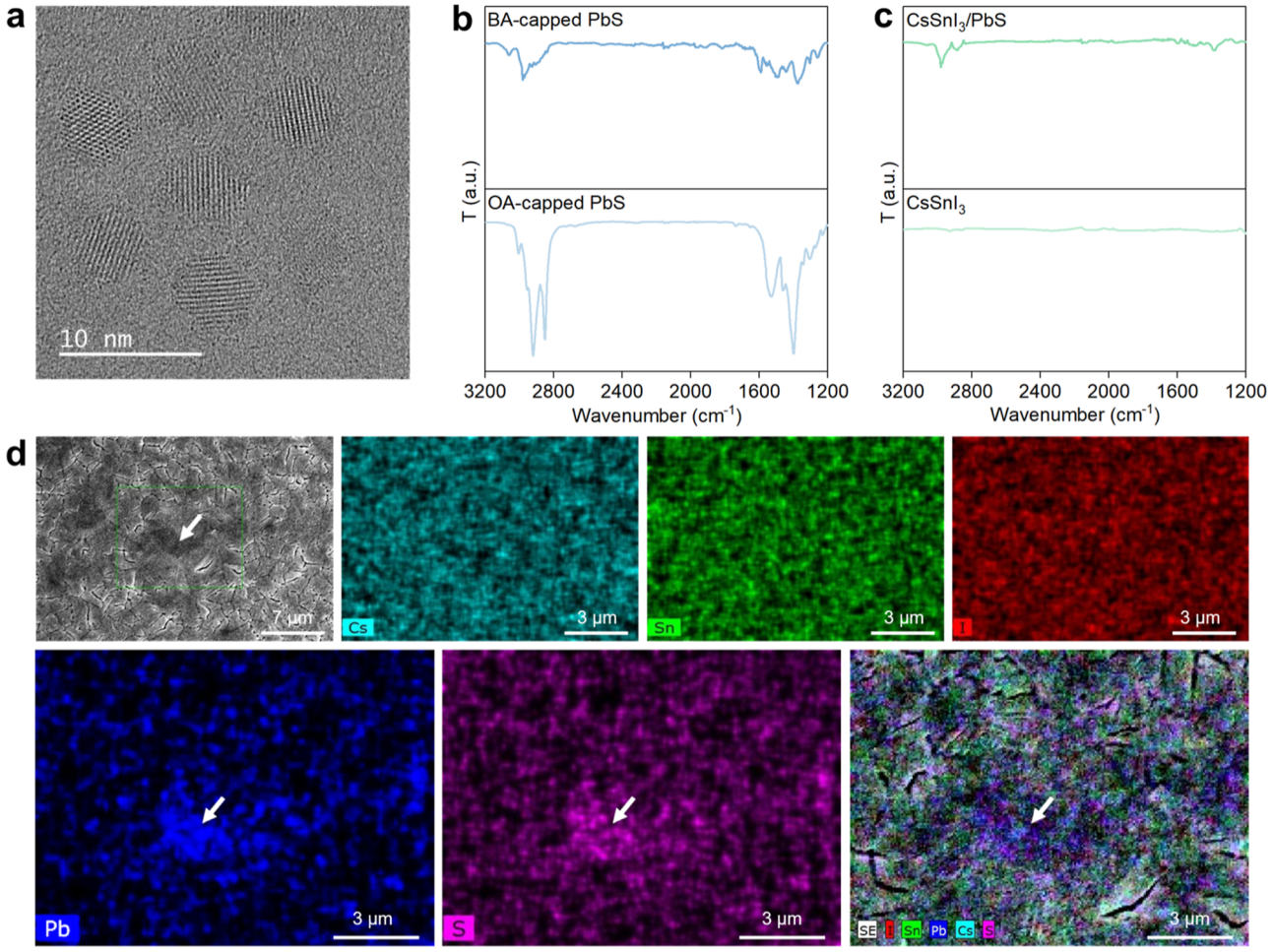

Figure 2. (a) HRTEM image of BA-stabilized PbS QDs. FTIR spectra of (b) PbS QD films with OA and BA ligands. (c) $CsSnI_3$ and $CsSnI_3$/PbS films. (d) SEM–EDX elemental mapping showing the distribution of Cs, Sn, I, Pb, and S elements in the $CsSnI_3$/PbS film. Area with the arrow shows the presence of Pb and S elements at the same spot in the mapping images, confirming the presence of PbS clusters.

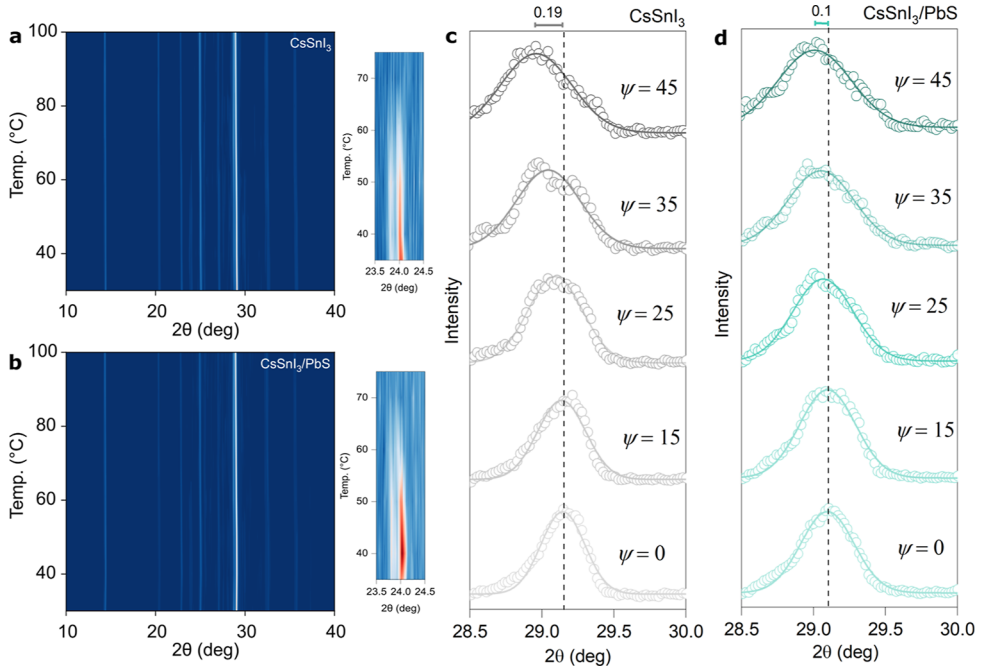

Figure 3. In situ temperature-dependent XRD of (a) $CsSnI_3$ (b) $CsSnI_3$/PbS films. Zoom-in view of the XRD peak representing phase transition is also shown in (a,b). GIXRD spectra at different tilt angles (ψ) for the (c) $CsSnI_3$ and (d) $CsSnI_3$/PbS films.

https://doi.org/10.1021/acsnano.4c09811
ACS Nano 2024, 18, 34089–34095

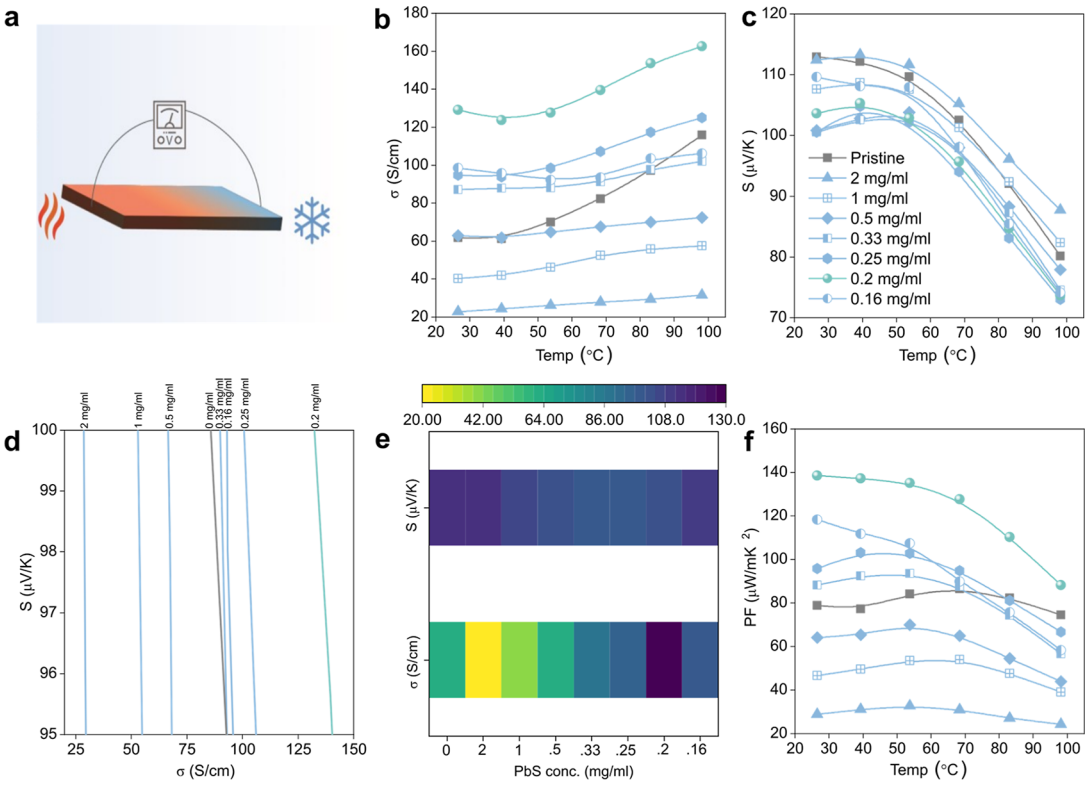

Figure 4. (a) Schematic of transport property measurement. Temperature-dependent (b) electrical conductivity and (c) Seebeck coefficient for different concentrations of PbS in $CsSnI_3$ matrix films. (d) Seebeck coefficient vs electrical conductivity curves as a function of PbS concentration in the $CsSnI_3$ matrix showing a minute change in the Seebeck coefficient between different DIM films. (e) Heat map showing RT electrical conductivity and Seebeck coefficient of $CsSnI_3$/PbS films. Colors indicate that for a stark change in the electrical conductivity, there is a minor change in the Seebeck coefficient. (f) Power factor (PF) of $CsSnI_3$/PbS films. Gray and green data points in figure represent pristine $CsSnI_3$ and best performing DIM $CsSnI_3$/PbS, respectively.

setup for σ and S. σ is measured by the 4-point measurement method, and S is measured in a dual Peltier configuration under a temperature gradient (details in the Experimental Section). The σ values of the $CsSnI_3$/PbS films decreased significantly for higher concentrations of PbS (2−0.5 mg/mL). For lower concentrations of PbS, σ started to increase with decreasing PbS concentration (Figure 4b), with the highest σ observed for 0.2 mg/mL PbS. A further decrease in the PbS concentration did not improve the σ value, as the concentration was too low to produce any significant effect.

S can provide important information on the carrier type and charge transport mechanisms as it is dependent on the energy distribution of carriers with respect to the Fermi level.[28] Temperature-dependent S confirms that $CsSnI_3$/PbS maintained the p-type nature of $CsSnI_3$ for different concentrations of PbS (Figure 4c). Interestingly, the decrease in S as a function of PbS concentration was small, while there was a 6.5-fold change in σ between the highest and lowest PbS concentrations (Figure 4d). 2D color map of σ and S at RT as a function of PbS concentration shows a negligible change in S (Figure 4e). There exists an anticorrelation between σ and S, where S decreases with increasing σ. Increasing carrier density (n) by doping, for instance, increases σ due to the direct relationship $\sigma = ne\mu$, where μ is mobility. However, S decreases in this process due to its inverse relation to n.[29,30] The unvarying behavior of S in the case of $CsSnI_3$/PbS indicates breaking of the σ−S trade-off, beneficial for thermoelectric applications. We calculated the PF, σS^2, to evaluate the thermoelectric performance (Figure 4f). The highest PF of 138 μW/m K^2 at RT was achieved for $CsSnI_3$/PbS with 0.2 mg/mL PbS, significantly higher than that for pristine $CsSnI_3$ (78 μW/m K^2). To evaluate the thermoelectric ZT of $CsSnI_3$ and $CsSnI_3$/PbS, in-plane thermal conductivity was measured by a chip-based 3ω technique (Figure S7a). The thermal conductivity (κ) of $CsSnI_3$/PbS is slightly lower than that of pristine $CsSnI_3$, which can be attributed to enhanced phonon scattering due to the presence of PbS.[31] This resulted in a ZT of 0.15 at RT (Figure S7b) for $CsSnI_3$/PbS. Table S1 summarizes the thermoelectric parameters of the $CsSnI_3$ and $CsSnI_3$/PbS films.

To further understand the decoupling of σ−S, we measured the carrier density at RT. Interestingly, the carrier density of $CsSnI_3$/PbS remains unchanged as a function of the PbS concentration, while the mobility is markedly affected (Figure S8). The mobility of $CsSnI_3$/PbS decreased and increased for higher and lower concentrations of PbS, respectively. To unravel the underlying mechanisms of the deviation in the mobility of $CsSnI_3$ films caused by different QD concentrations, we used DFT to explore the effective masses of $CsSnI_3$ at various QD concentrations. We hypothesized that the QD effects are achieved through the different strains they introduce into the systems, manifesting as deviations in the lattice vectors and corresponding unit cell volumes. To mimic these strain effects, the lattice constants are fixed to the experimentally determined values, and the corresponding atomic positions are fully relaxed by PBE + TS (more details can be found in the Supporting Information). The HSE06 +

https://doi.org/10.1021/acsnano.4c09811
ACS Nano 2024, 18, 34089−34095

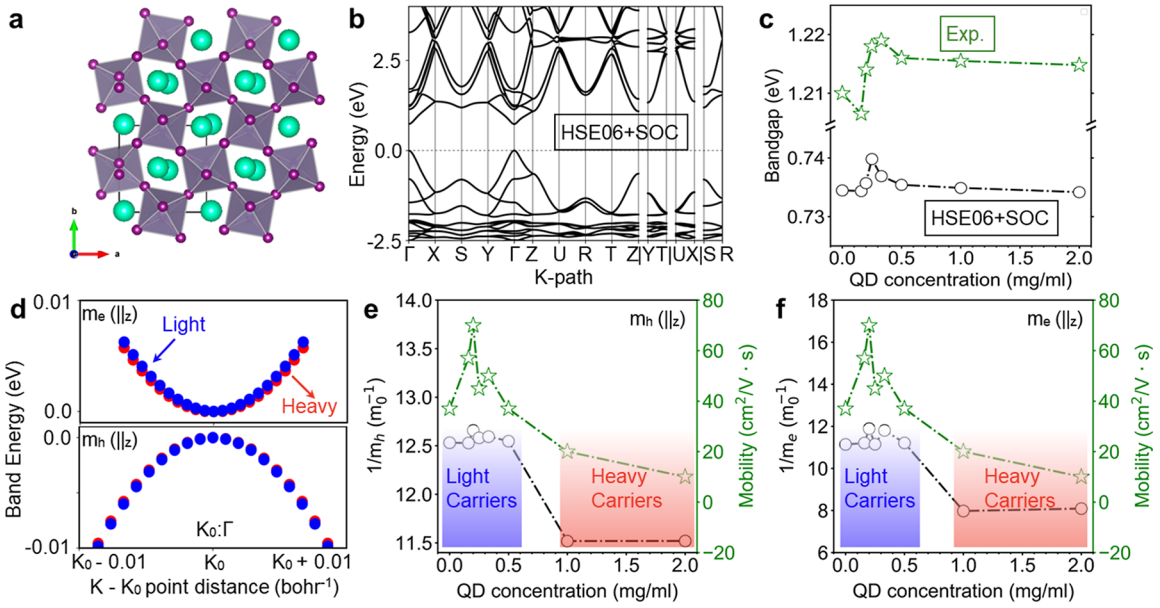

Figure 5. (a) Crystal structure of $CsSnI_3$ without QD and (b) corresponding HSE06 + SOC calculated band structures. (c) Bandgap of $CsSnI_3$ within different QD concentrations obtained by the HSE06 + SOC (black) and experiments (green). (d) Degenerate bands around the Γ point along the z direction [$\|_z$ parallel to the reciprocal z-axis in the conventional cell as shown in (a)] for electrons and holes which the corresponding effective mass can be obtained through the parabolic fits to those calculated band structures at valence band maximum and conduction band minimum (Γ points), the heavy and light carriers are labeled as red and blue, respectively, the inverse of the (e) hole effective mass ($1/m_h$) and (f) electron effective mass ($1/m_e$) along the z direction (parallel to the reciprocal z-axis in the conventional cell) obtained via HSE06 + SOC calculated band energies, and the carrier mobility (green) obtained through experimental techniques. In figure (e,f), the heavy and light carrier dominant regions are labeled red and blue, respectively. Thus, in the light carrier region, the theory results are obtained based on the light carriers. In the heavy carrier region, the theory results are obtained based on the heavy carriers. More details can be found in Figure S10. The values are presented in units of the inverse of the free electron mass, $1/m_0$.

SOC band structures (Figure 5a,b) were subsequently calculated for $CsSnI_3$.

The trends of the bandgap changes under different QD concentrations (Figure 5c) are well captured by theory compared to the experimental results (Figure S9), which also proves the accuracy and rationality of the atomic structures we used for $CsSnI_3$ under different QD concentrations. Finally, the effective masses are further calculated through parabolic fits to the calculated band structures around the band extrema following previously reported strategies.[32] As the bands are degenerate (Figure 5d) around the band extrema (Γ point), there exist heavy and light carriers which dominate the system carrier transport within short diffusion lengths and long diffusion lengths, respectively. Although slight differences exist in the effective mass values along different directions (e.g., $\|_x$, $\|_y$, and $\|_z$, shown in Figure S9), the trends predicted by adding the QDs are almost the same. As a result, in the latter, we focus only on the trends in the z direction ($\|_z$). We found that the inverse of the effective masses ($1/m_h$, $1/m_e$) of light and heavy carriers showed completely opposite trends when QDs were added (Figure S10), and neither of these trends agreed with the experimentally observed trends of mobility. However, perfect agreement between the theoretically predicted and experimentally determined mobility can be achieved by considering the transition from light carriers to heavy carriers while adding QDs (Figure 5e,f). We hypothesized that when the QD concentration is low (e.g., 0, 0.16, 0.25, 0.33, and 0.5 mg/mL), the introduced QDs will not decrease the diffusion length of the system. As a result, light holes/electrons will dominate the overall transport properties. For higher concentration of QDs (e.g., 1.0 and 2.0 mg/mL), it may decrease the system diffusion length, and the heavy holes/electrons begin to dominate. Understanding the effects of light and heavy carriers as well as strain on halide perovskites can aid in designing better devices. DFT can be used as a screening tool to first determine the optimal strain and secondary material phase that should be introduced into the system and its effect on resulting carrier transport properties. Application-specific designed DIMs have the potential to offer longer diffusion length, higher mobility, faster response times along with improved stability for various applications such as solar cells, photodetectors, and thermoelectrics.

Several works have demonstrated enhanced stability in DIM compared with pristine QDs or halide perovskites alone. Such improvement is particularly important in the present case, as $CsSnI_3$ tends to undergo structural changes at RT. Black 3D $CsSnI_3$ can transform to yellow phase 1D $Cs_2Sn_2I_6$. To assess the improvement in the stability of $CsSnI_3$ by PbS incorporation, we measured σ after storing the sample in a sealed vial for 200 h. Pristine $CsSnI_3$ changed its color to yellow, while the $CsSnI_3$/PbS film maintained its black color, underscoring the enhanced phase stability (Figure S11).

CONCLUSIONS

In summary, the chalcogenide QD-in-perovskite matrix shows improved and tunable electrical conductivity. The tensile strain of the DIM film was reduced by the inclusion of PbS in $CsSnI_3$, resulting in improved phase stability. Enhanced carrier mobility was observed in DIM owing to different transport regimes dominated by light or heavy carriers as a function of QD concentration, leading to the breaking of conductivity–Seebeck trade-off. High-room-temperature PF was demon-

https://doi.org/10.1021/acsnano.4c09811
ACS Nano 2024, 18, 34089−34095

strated in DIM, offering a material system for further exploration of room-temperature halide perovskite-based thermoelectrics.

METHODS/EXPERIMENTAL SECTION

Materials. SnI_2 (99.99%), CsI (99.999%), DMF, DMSO, and chlorobenzene were purchased from Sigma-Aldrich and were used as received unless otherwise stated.

Sample Preparation. BA-capped PbS QDs were synthesized as per a previous report.[24] To prepare the perovskite precursor solution, CsI and SnI_2 with the required molar ratios were dissolved in DMF and DMSO (a volume ratio of 8:2) with a total concentration of 1.3 M and stirred at room temperature. Pristine $CsSnI_3$ films were prepared on glass by spin coating the precursor solution at 1000 rpm for 10 s and 4000 rpm for 30 s in an N_2 glovebox. 100 μL of chlorobenzene was dripped on the spinning substrate after the first 18 s of the spin-coating process. The spin-coated films were annealed at 50 °C for 20 min and then at 100 °C for 20 min. For and $CsSnI_3$/QD films, 100 μL of chlorobenzene with different concentrations of PbS QDs was dripped on $CsSnI_3$. The thickness of all films was ~400 nm.

Material Characterization. SEM images and energy-dispersive X-ray spectroscopy (EDX) analysis were obtained using a Thermo Fisher Nova Nano SEM equipped with an AMETEK EDAX SDD detector. TEM investigations were performed with a Thermo Fisher Titan Cs-Image microscope equipped with a spherical aberration corrector for the objective lens. XRD patterns were obtained from a Bruker D8 ADVANCE diffractometer. Lattice parameters were estimated by the UnitCell program using the XRD data.[33] 2D XRD measurements were carried out on a Bruker D8 Discover system equipped with the IμS point focus Cu-source and a multimode Eiger2 R 500 K 2D detector. For the strain measurements, we fixed the 2θ and varied the instrument tilt angle ψ to obtain the corresponding XRD patterns. UV−vis absorption spectra were recorded by using a Perkin-Lambda spectrometer. Fourier transform infrared (FTIR) spectra were recorded using a Thermo Scientific attenuated total reflection-FTIR spectrometer.

Thermoelectric Measurements. Electrical conductivity and Seebeck measurements were performed on a Netzsch SBA 548 Nemesis thermoelectric set up under a He environment using a four-probe technique and dual Peltier configuration, respectively. Fresh samples were measured by transferring from the glovebox to a thermoelectric setup in less than 30 s under a N_2 shower. The instrument uncertainties for electrical conductivity and Seebeck measurements are ±5% and ±7%, respectively. Charge carrier concentration was measured in van der Pauw geometry on the Lakeshore Hall system at RT under a N_2 flow. The hole mobility was calculated by combining the electrical conductivity and charge carrier concentration using the relation $\mu = \sigma/ne$.[34] In-plane thermal conductivity was measured under vacuum using the 3ω Völklein method, with a Linseis thin-film analyzer.[35] Samples were spin-coated onto prepatterned test chips from Linseis.

ASSOCIATED CONTENT

Supporting Information

The Supporting Information is available free of charge at https://pubs.acs.org/doi/10.1021/acsnano.4c09811.

Additional XRD, TEM, and SEM, electrical transport properties, DFT methodology, and electrical stability (PDF)

AUTHOR INFORMATION

Corresponding Authors

Edward H. Sargent − *Department of Electrical and Computer Engineering, University of Toronto, Toronto, Ontario M5S 1A4, Canada;* orcid.org/0000-0003-0396-6495; Email: ted.sargent@utoronto.ca

Derya Baran − *Material Science and Engineering Program (MSE), Physical Sciences and Engineering Division (PSE), King Abdullah University of Science and Technology (KAUST), Thuwal 23955-6900, Kingdom of Saudi Arabia;* orcid.org/0000-0003-2196-8187; Email: derya.baran@kaust.edu.sa

Authors

Md Azimul Haque − *Material Science and Engineering Program (MSE), Physical Sciences and Engineering Division (PSE), King Abdullah University of Science and Technology (KAUST), Thuwal 23955-6900, Kingdom of Saudi Arabia;* orcid.org/0000-0003-3528-0674

Tong Zhu − *Department of Electrical and Computer Engineering, University of Toronto, Toronto, Ontario M5S 1A4, Canada*

Roba Tounesi − *Material Science and Engineering Program (MSE), Physical Sciences and Engineering Division (PSE), King Abdullah University of Science and Technology (KAUST), Thuwal 23955-6900, Kingdom of Saudi Arabia*

Seungjin Lee − *Department of Electrical and Computer Engineering, University of Toronto, Toronto, Ontario M5S 1A4, Canada;* orcid.org/0000-0002-6318-0702

Maral Vafaie − *Department of Electrical and Computer Engineering, University of Toronto, Toronto, Ontario M5S 1A4, Canada;* orcid.org/0000-0001-9119-6499

Luis Huerta Hernandez − *Material Science and Engineering Program (MSE), Physical Sciences and Engineering Division (PSE), King Abdullah University of Science and Technology (KAUST), Thuwal 23955-6900, Kingdom of Saudi Arabia*

Bambar Davaasuren − *Corelabs, King Abdullah University of Science and Technology (KAUST), Thuwal 23955-6900, Saudi Arabia*

Alessandro Genovese − *Corelabs, King Abdullah University of Science and Technology (KAUST), Thuwal 23955-6900, Saudi Arabia*

Complete contact information is available at: https://pubs.acs.org/10.1021/acsnano.4c09811

Author Contributions

[‖]M.A.H. and T.Z. contributed equally to this work.

Notes

The authors declare no competing financial interest.

ACKNOWLEDGMENTS

This publication was supported by the King Abdullah University of Science and Technology (KAUST) Office of Sponsored Research (OSR) under Award No. OSR-CRG2018-3737. Figures 1 and 4a were created by Ana Bigio, scientific illustrator at KAUST.

REFERENCES

(1) Liu, M.; Chen, Y.; Tan, C. S.; Quintero-Bermudez, R.; Proppe, A. H.; Munir, R.; Tan, H.; Voznyy, O.; Scheffel, B.; Walters, G.; Kam, A. P. T.; Sun, B.; Choi, M. J.; Hoogland, S.; Amassian, A.; Kelley, S. O.; Garcia de Arquer, F. P.; Sargent, E. H. Lattice Anchoring Stabilizes Solution-Processed Semiconductors. *Nature* **2019**, *570*, 96−101.

(2) Zhou, S.; Tang, R.; Yin, L. Slow-Photon-Effect-Induced Photoelectrical-Conversion Efficiency Enhancement for Carbon-Quantum-Dot-Sensitized Inorganic CsPbBr(3) Inverse Opal Perovskite Solar Cells. *Adv. Mater.* **2017**, *29*, 1703682.

(3) Gao, L.; Quan, L. N.; García de Arquer, F. P.; Zhao, Y.; Munir, R.; Proppe, A.; Quintero-Bermudez, R.; Zou, C.; Yang, Z.; Saidaminov, M. I.; Voznyy, O.; Kinge, S.; Lu, Z.; Kelley, S. O.; Amassian, A.; Tang, J.; Sargent, E. H. Efficient near-Infrared Light-Emitting Diodes Based on Quantum Dots in Layered Perovskite. *Nat. Photonics* **2020**, *14*, 227−233.
(4) Garcia de Arquer, F. P.; Gong, X.; Sabatini, R. P.; Liu, M.; Kim, G. H.; Sutherland, B. R.; Voznyy, O.; Xu, J.; Pang, Y.; Hoogland, S.; Sinton, D.; Sargent, E. Field-Emission from Quantum-Dot-in-Perovskite Solids. *Nat. Commun.* **2017**, *8*, 14757.
(5) Conley, A. M.; Sarabamoun, E. S.; Dagnall, K. A.; Yoon, L. U.; Rajeev, H. S.; Lee, S.-H.; Choi, J. J. Quantum-Dot-Doped Lead Halide Perovskites for Ionizing Radiation Detection. *ACS Appl. Opt. Mater.* **2023**, *1*, 715−723.
(6) Liu, S.; Chen, Y.; Gao, W.; Li, W.; Yang, X.; Li, Z.; Xiao, Z.; Liu, Y.; Wang, Y. Epitaxy of a Monocrystalline Cspbbr(3) -Srtio(3) Halide-Oxide Perovskite P-N Heterojunction with High Stability for Photodetection. *Adv. Mater.* **2023**, *35*, No. e2303544.
(7) Williams, R. T.; Wolszczak, W. W.; Yan, X.; Carroll, D. L. Perovskite Quantum-Dot-in-Host for Detection of Ionizing Radiation. *ACS Nano* **2020**, *14*, 5161−5169.
(8) Ning, Z.; Gong, X.; Comin, R.; Walters, G.; Fan, F.; Voznyy, O.; Yassitepe, E.; Buin, A.; Hoogland, S.; Sargent, E. H. Quantum-Dot-in-Perovskite Solids. *Nature* **2015**, *523*, 324−328.
(9) Rakshit, S.; Piatkowski, P.; Mora-Seró, I.; Douhal, A. Combining Perovskites and Quantum Dots: Synthesis, Characterization, and Applications in Solar Cells, Leds, and Photodetectors. *Adv. Opt. Mater.* **2022**, *10*, 2102566.
(10) Bessonov, A. A.; Allen, M.; Liu, Y.; Malik, S.; Bottomley, J.; Rushton, A.; Medina-Salazar, I.; Voutilainen, M.; Kallioinen, S.; Colli, A.; Bower, C.; Andrew, P.; Ryhanen, T. Compound Quantum Dot-Perovskite Optical Absorbers on Graphene Enhancing Short-Wave Infrared Photodetection. *ACS Nano* **2017**, *11*, 5547−5557.
(11) Hunsur Ravikumar, C.; Maroli, N.; Kulkarni, B.; Kolandaivel, P.; Balakrishna, R. G. Heterostructure of Cspbbr3-Cds Perovskite Quantum Dots for Enhanced Stability and Charge Transfer. *Mater. Sci. Eng., B* **2022**, *275*, 115513.
(12) Han, J.; Yin, X.; Nan, H.; Zhou, Y.; Yao, Z.; Li, J.; Oron, D.; Lin, H. Enhancing the Performance of Perovskite Solar Cells by Hybridizing Sns Quantum Dots with Ch(3) Nh(3) Pbi(3). *Small* **2017**, *13*, 1700953.
(13) Gaulding, E. A.; Chen, X.; Yang, Y.; Harvey, S. P.; To, B.; Kim, Y.-H.; Beard, M. C.; Sercel, P. C.; Luther, J. M. Embedding Pbs Quantum Dots (Qds) in Pb-Halide Perovskite Matrices: Qd Surface Chemistry and Antisolvent Effects on Qd Dispersion and Confinement Properties. *ACS Mater. Lett.* **2020**, *2*, 1464−1472.
(14) Zhao, C.; Chen, C.; Wei, R.; Zou, Y.; Kong, W.; Huang, T.; Yu, Z.; Yang, J.; Li, F.; Han, Y.; Guo, C.; Yu, W. Laser-Assisted Synthesis of Ag2s-Quantum-Dot-in-Perovskite Matrix and Its Application in Broadband Photodetectors. *Adv. Opt. Mater.* **2021**, *10*, 2101535.
(15) Quintero-Bermudez, R.; Sabatini, R. P.; Lejay, M.; Voznyy, O.; Sargent, E. H. Small-Band-Offset Perovskite Shells Increase Auger Lifetime in Quantum Dot Solids. *ACS Nano* **2017**, *11*, 12378−12384.
(16) Masi, S.; Echeverría-Arrondo, C.; Salim, K. M. M.; Ngo, T. T.; Mendez, P. F.; López-Fraguas, E.; Macias-Pinilla, D. F.; Planelles, J.; Climente, J. I.; Mora-Seró, I. Chemi-Structural Stabilization of Formamidinium Lead Iodide Perovskite by Using Embedded Quantum Dots. *ACS Energy Lett.* **2020**, *5*, 418−427.
(17) Shi, Y.; Yuan, L.; Liu, Z.; Lu, Y.; Yuan, B.; Shen, W.; Xue, B.; Zhang, Y.; Qian, Y.; Li, F.; Zhang, X.; Liu, Y.; Wang, Y.; Wang, L.; Yuan, J.; Liao, L. S.; Yang, B.; Yu, Y.; Ma, W. In Situ Growth of Strained Matrix on Cspbi(3) Perovskite Quantum Dots for Balanced Conductivity and Stability. *ACS Nano* **2022**, *16*, 10534−10544.
(18) Ngo, T. T.; Masi, S.; Mendez, P. F.; Kazes, M.; Oron, D.; Sero, I. M. Pbs Quantum Dots as Additives in Methylammonium Halide Perovskite Solar Cells: The Effect of Quantum Dot Capping. *Nanoscale Adv.* **2019**, *1*, 4109−4118.
(19) Qin, M.; Li, Y.; Yang, Y.; Chan, P. F.; Li, S.; Qin, Z.; Guo, X.; Shu, L.; Zhu, Y.; Fan, Z.; Su, C.-J.; Lu, X. Regulating the Crystallization Kinetics and Lattice Strain of Lead-Free Perovskites with Perovskite Quantum Dots. *ACS Energy Lett.* **2022**, *7*, 3251−3259.
(20) Haque, M. A.; Zhu, T.; Hernandez, L. H.; Tounesi, R.; Combe, C.; Davaasuren, B.; Emwas, A.-H.; García de Arquer, F. P.; Sargent, E. H.; Baran, D. Electrical Tunability of Inorganic Tin Perovskites Enabled by Organic Modifiers. *Cell. Rep. Phys. Sci.* **2023**, *4*, 101703.
(21) Liu, A.; Zhu, H.; Bai, S.; Reo, Y.; Zou, T.; Kim, M.-G.; Noh, Y.-Y. High-Performance Inorganic Metal Halide Perovskite Transistors. *Nat. Electron.* **2022**, *5*, 78−83.
(22) Liu, T.; Zhao, X.; Li, J.; Liu, Z.; Liscio, F.; Milita, S.; Schroeder, B. C.; Fenwick, O. Enhanced Control of Self-Doping in Halide Perovskites for Improved Thermoelectric Performance. *Nat. Commun.* **2019**, *10*, 5750.
(23) Haque, M. A.; Rosas Villalva, D.; Hernandez, L. H.; Tounesi, R.; Jang, S.; Baran, D. Role of Dopants in Organic and Halide Perovskite Energy Conversion Devices. *Chem. Mater.* **2021**, *33*, 8147−8172.
(24) Lee, S.; Choi, M. J.; Sharma, G.; Biondi, M.; Chen, B.; Baek, S. W.; Najarian, A. M.; Vafaie, M.; Wicks, J.; Sagar, L. K.; Hoogland, S.; de Arquer, F. P. G.; Voznyy, O.; Sargent, E. H. Orthogonal Colloidal Quantum Dot Inks Enable Efficient Multilayer Optoelectronic Devices. *Nat. Commun.* **2020**, *11*, 4814.
(25) Haque, M. A.; Hernandez, L. H.; Davaasuren, B.; Villalva, D. R.; Troughton, J.; Baran, D. Tuning the Thermoelectric Performance of Hybrid Tin Perovskites by Air Treatment. *Adv. Energy Sustainability Res.* **2020**, *1*, 2000033.
(26) Liang, H.; Yang, W.; Xia, J.; Gu, H.; Meng, X.; Yang, G.; Fu, Y.; Wang, B.; Cai, H.; Chen, Y.; Yang, S.; Liang, C. Strain Effects on Flexible Perovskite Solar Cells. *Adv. Sci.* **2023**, *10*, No. e2304733.
(27) Zhu, C.; Niu, X.; Fu, Y.; Li, N.; Hu, C.; Chen, Y.; He, X.; Na, G.; Liu, P.; Zai, H.; Ge, Y.; Lu, Y.; Ke, X.; Bai, Y.; Yang, S.; Chen, P.; Li, Y.; Sui, M.; Zhang, L.; Zhou, H.; Chen, Q. Strain Engineering in Perovskite Solar Cells and Its Impacts on Carrier Dynamics. *Nat. Commun.* **2019**, *10*, 815.
(28) Liang, Z.; Choi, H. H.; Luo, X.; Liu, T.; Abtahi, A.; Ramasamy, U. S.; Hitron, J. A.; Baustert, K. N.; Hempel, J. L.; Boehm, A. M.; Ansary, A.; Strachan, D. R.; Mei, J.; Risko, C.; Podzorov, V.; Graham, K. R. N-Type Charge Transport in Heavily P-Doped Polymers. *Nat. Mater.* **2021**, *20*, 518−524.
(29) Wang, P. L.; Kolodiazhnyi, T.; Yao, J.; Mozharivskyj, Y. Decoupling the Electrical Conductivity and Seebeck Coefficient in the Re2sbo2 Compounds through Local Structural Perturbations. *J. Am. Chem. Soc.* **2012**, *134*, 1426−1429.
(30) Zhu, T.; Liu, Y.; Fu, C.; Heremans, J. P.; Snyder, J. G.; Zhao, X. Compromise and Synergy in High-Efficiency Thermoelectric Materials. *Adv. Mater.* **2017**, *29*, 1605884.
(31) Kim, W.; Zide, J.; Gossard, A.; Klenov, D.; Stemmer, S.; Shakouri, A.; Majumdar, A. Thermal Conductivity Reduction and Thermoelectric Figure of Merit Increase by Embedding Nanoparticles in Crystalline Semiconductors. *Phys. Rev. Lett.* **2006**, *96*, 045901.
(32) Zhu, T.; Huhn, W. P.; Wessler, G. C.; Shin, D.; Saparov, B.; Mitzi, D. B.; Blum, V. I2−Ii−Iv−Vi4 (I = Cu, Ag; Ii = Sr, Ba; Iv = Ge, Sn; Vi = S, Se): Chalcogenides for Thin-Film Photovoltaics. *Chem. Mater.* **2017**, *29*, 7868−7879.
(33) Weber, S. *RSD-PLOT*: a program for plotting Rietveld refinement data. *J. Appl. Crystallogr.* **1997**, *30*, 84−85.
(34) Stoumpos, C. C.; Malliakas, C. D.; Kanatzidis, M. G. Semiconducting Tin and Lead Iodide Perovskites with Organic Cations: Phase Transitions, High Mobilities, and near-Infrared Photoluminescent Properties. *Inorg. Chem.* **2013**, *52*, 9019−9038.
(35) Linseis, V.; Völklein, F.; Reith, H.; Nielsch, K.; Woias, P. Advanced Platform for the in-Plane Zt Measurement of Thin Films. *Rev. Sci. Instrum.* **2018**, *89*, 015110.

https://doi.org/10.1021/acsnano.4c09811
ACS Nano 2024, 18, 34089−34095